Measurement of Slip Length on Superhydrophobic Surfaces

Abdelhamid Maali, Bharat Bhushan

Measurement of slip length on superhydrophobic surfaces

By A. Maali[1,*] and B. Bhushan[2,*]

[1]*Laboratoire Ondes et Matière d'Aquitaine (LOMA), Université Bordeaux I, 351 cours de la Liberation, Talence 33405, France*
[2]*Nanoprobe Laboratory for Bio- and Nanotechnology and Biomimetics (NLB^2), Ohio State University, 201 W. 19th Avenue, Columbus, OH 43210-1142, USA*

In this paper, a review of different techniques used to measure the slip length on superhydrophobic surfaces with large slip length is presented. First, we present the theoretical models used to calculate the effective slip length on superhydrophobic surfaces in different configurations of liquid flow. Then, we present the different techniques used to measure the slip past these superhydrophobic surfaces: rheometry, particle image velocimetry, pressure drop, surface force apparatus and atomic force microscopy.

Keywords: fluid slip; atomic force microscopy; surface force apparatus; rheometry; particle image velocimetry; pressure drop

1. Introduction

Liquid flow close to the interface has received much attention recently, and it has been studied theoretically and experimentally by several groups. Using the newly developed techniques, it is actually possible to drive and probe the flow at the micro/nanoscales. For a smooth hydrophobic surface, there is an agreement that the fluid flow is subject to a slip close to the boundary [1–5]. The amount of fluid slip is commonly represented by the slip b, which is typically of the order of tens of nanometres. Very large slip length has been reported on superhydrophobic surfaces [6–8]. Large slip length indicates that the liquid flow between confining surfaces experiences a lower friction, and a solid moving in a liquid experiences a lower drag force. Therefore, to create surfaces that increase slip length becomes a hot topic in micro/nanofluidics devices.

In this paper, various techniques used to measure drag and slip length on micro/nanostructured superhydrophobic surfaces with large slip length are reviewed. Some theoretical models and calculated expressions for the effective slip length on the superhydrophobic surface are presented first. Next, the different techniques to measure the slip length are presented. This review is divided into

*Authors for correspondence (a.maali@loma.u-bordeaux1.fr; bhushan.2@osu.edu).

One contribution of 10 a Theme Issue 'Biosensors: surface structures and materials'.

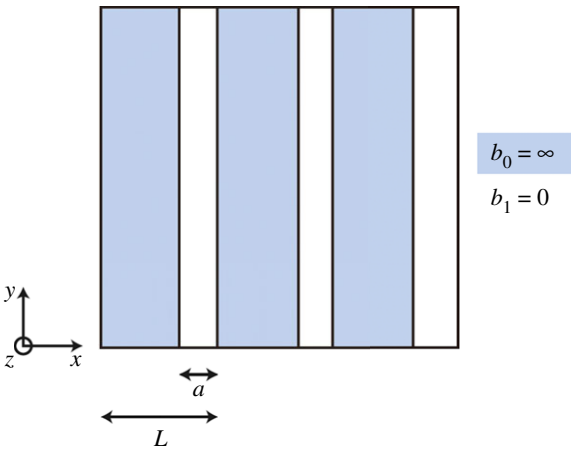

Figure 1. Schematic of the microscopic hydrodynamic boundary condition, alternating stripes of slip length b_0 and slip length b_1. Adapted from [12]. (Online version in colour.)

three sections. In §2, models and theoretical calculations of the effective slip length on structured superhydrophobic surface are presented. In §3, various techniques to measure large slip length, which include rheometry, particle image velocimetry, pressure-drop, surface force apparatus (SFA) and atomic force microscope (AFM) measurements, and some representative results are presented. In §4, a summary and outlook are provided.

2. Calculation of the effective slip length

As mentioned earlier, several groups have theoretically investigated liquid flow on superhydrophobic surfaces. They have calculated the effective slip length in different situations. Here, the simplest models are recalled, and their results are presented.

A planar surface with one-dimensional features, such as long grooves, usually aligned or perpendicular parallel to the flow directions has been studied by several authors. Philip [9,10] studied the flow in a pipe of radius R with stripes parallel to the flow. In such situations, the pipe surface is patterned with a periodic no-slip and slip region. When $R \to \infty$, the effective slip length is given by

$$b_{\text{Philip}} = \frac{L}{\pi} \ln\left(\cos\left(\frac{\pi\phi_g}{2}\right)\right), \tag{2.1}$$

where L is the pitch of the pattern and ϕ_g is the gas fraction area (fraction of the surface where the slip is infinity). ϕ_g is equal to $(L-a)/L$, where a is the stripe width with zero slip length. For similar surfaces, but with a pattern perpendicular to the flow, Lauga & Stone [11] calculated the slip length, and when the radius of the pipe $R \to \infty$, their expression is reduced to

$$b_{\text{Lauga-Stone}} = \frac{L}{2\pi} \ln\left(\cos\left(\frac{\pi\phi_g}{2}\right)\right). \tag{2.2}$$

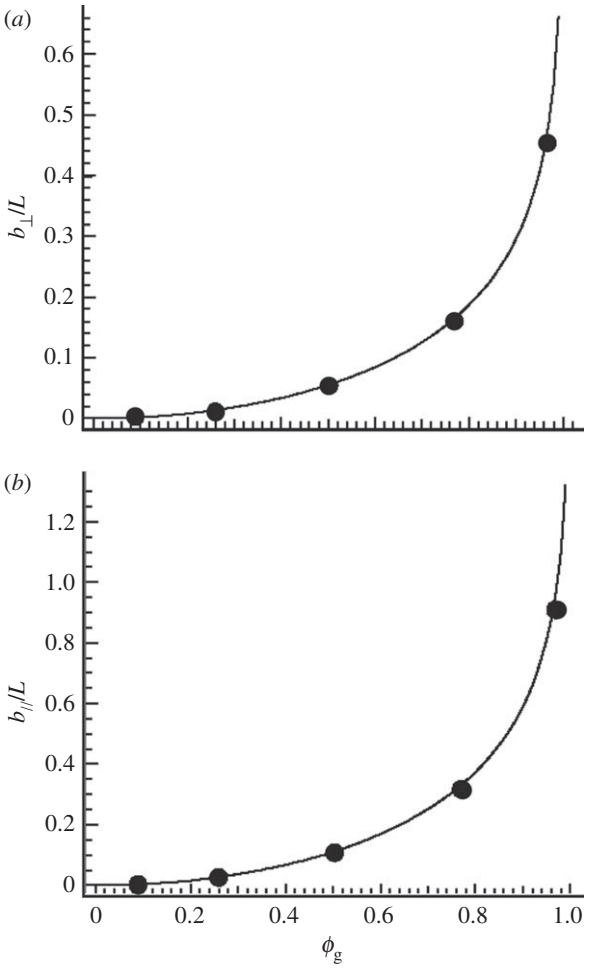

Figure 2. The effective slip length b as a function of the gas fraction area $\phi_g = (L - a)/L$ (fraction of the surface where the slip is infinity). The curves represent the analytical calculations and the circles the semi-analytical calculation: (a) flow perpendicular to the stripes and (b) flow parallel to the stripes. Reproduced with permission from [12].

Cottin-Bizonne *et al.* [12] conducted semi-analytical calculations to calculate the effective slip length on microstructured superhydrophobic surfaces. A schematic of their situation is presented in figure 1. They solved the Navier–Stokes equation and calculated effective slip length defined as $b = V_s/\dot{\gamma}$, where V_S is the effective velocity slip on the surface and $\dot{\gamma}$ is the shear rate that is imposed at an infinite distance from the surface. They considered first a surface composed of a succession of stripes of width a characterized by a slip length ($b_1 = 0$) and stripes of width $L - a$ having an infinite slip length ($b_0 \to \infty$). The results are presented in figure 2 for the case of flow parallel to the stripes (figure 2a) and perpendicular to the stripes (figure 2b). As shown in figure 2, their approach is in excellent agreement with the analytical results of Philip [9] (flow parallel to stripes) and Lauga & Stone [11] (flow perpendicular to stripes).

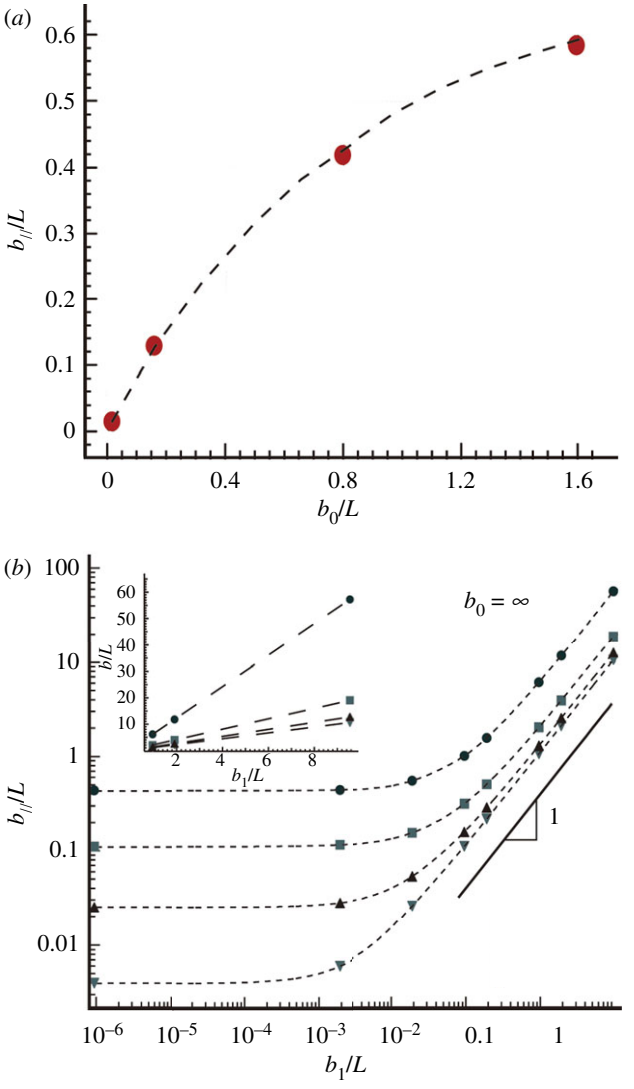

Figure 3. (a) Effective slip length b on a surface composed of alternating stripes with slip length b_0 and vanishing slip length ($b_1 = 0$) as a function of the slip length b_0 (the gas fraction area is $\phi_g = 97\%$) and (b) effective slip length b on a surface composed of alternating stripes with slip length b_1 and infinite slip length $b_0 \to \infty$. The semi-analytical calculation was carried out for different values of gas fraction area ϕ_g. The short-dashed lines are a guide to the eye. In the inset, the same points are plotted on a linear scale. The dashed lines are linear fits to the measured values of b. The shear flow in both cases is parallel to the stripes. Reproduced with permission from [12]. Circles, $\phi_g = 0.833$; squares, $\phi_g = 0.5$; triangles, $\phi_g = 0.25$; inverted triangles, $\phi_g = 0.1$. (Online version in colour.)

They also studied two other particular cases: one was a surface composed of alternating stripes of no-slip ($b_1 = 0$) and partial-slip length (b_0) and the second was a surface composed of alternating stripes of infinite-slip ($b_0 \to \infty$) and partial-slip length (b_1). Figure 3a,b shows the evolution of the macroscopic slip length b as a function of the microscopic slip length b_0 and b_1, respectively.

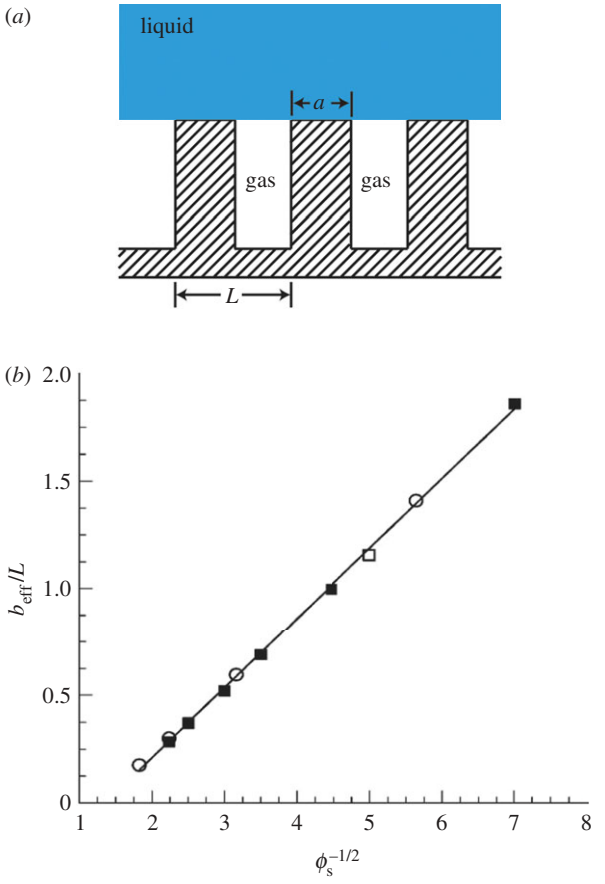

Figure 4. (*a*) Schematic of the liquid interface in a surface with two-dimensional patterning with posts organized on a square lattice. (*b*) Normalized effective slip length b_{eff}/L for a composite surface plotted against $1/\sqrt{\phi_{\mathrm{s}}}$. The solid line represents the linear regression ($b_{\mathrm{eff}}/L = 0.325/\sqrt{\phi_{\mathrm{s}}} - 0.44$). Reproduced with permission from [13]. (Online version in colour.)

A surface with two-dimensional patterning, usually composed of a series of posts distributed on a regular lattice as illustrated in figure 4*a*, is expected to display lower friction than a surface with one-dimensional patterning. Ybert *et al.* [13] were the first to calculate an expression that predicted the value of the effective slip length for the given surface. Their results are based on semi-analytical calculations, as mentioned above. They computed the effective slip length as a function of the solid fraction (surface area where the slip length vanishes). Then, a linear regression was performed on the numerical calculated data that allows extraction of a useful and very simple expression for the effective slip length b_{eff} as function of the solid fraction ϕ_{s},

$$b_{\mathrm{eff}} = L\left(\frac{0.325}{\sqrt{\phi_{\mathrm{s}}}} - 0.44\right). \tag{2.3}$$

In figure 4*b*, the computed effective slip length divided by L, where $\phi_{\mathrm{s}} = 1 - \phi_{\mathrm{g}} = a/L$, is plotted for different values of the solid fractions ϕ_{s}.

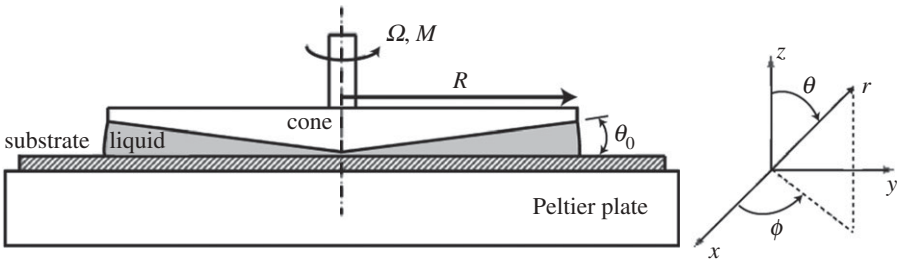

Figure 5. Schematic of a cone-and-plate rheometer, showing geometric parameters and reference frames. Reproduced with permission from [19].

Davis & Lauga [14] conducted analytical calculations to derive an expression of the effective slip length on the superhydrophobic surface composed of posts suitably distributed on a surface. For posts on a square lattice and in the limit of small coverage by the post (small solid fraction area), the value of the slip length can be obtained analytically. Their expression predicts that the relation between the slip length and the solid fraction is given by

$$b_{\text{eff}} = L\left(\frac{3}{16}\sqrt{\frac{\pi}{\phi_{\text{s}}}} - \frac{3}{2\pi}\ln(1+\sqrt{2})\right) \approx L\left(\frac{0.332}{\sqrt{\phi_{\text{s}}}} - 0.421\right). \tag{2.4}$$

Notice here the good agreement between the expression derived by Davis & Lauga [14] using analytical calculations and the expression derived by Ybert *et al.* [13] using numerical calculations.

3. Measurement methods and results

(*a*) *Rheometry experiments*

In such experiments, the slip length was obtained through torque measurements with a rheometer [15–18]. In figure 5, the schematic of a cone-plate rheometer is shown; this is the most popular geometry because it produces a uniform shear rate over the sample. When a cone of radius R with a very small angle θ_0 rotates at angular velocity Ω, the slip length is related to the measured torque by

$$M = \frac{2\pi\eta\Omega R^3}{3\theta_0}\left[1 - \frac{3b_{\text{eff}}}{2R\theta_0} + \frac{3b_{\text{eff}}^2}{R^2\theta_0^2} - \frac{3b_{\text{eff}}^3}{R^3\theta_0^3}\ln\left(\frac{R\theta_0 + b_{\text{eff}}}{b_{\text{eff}}}\right)\right], \tag{3.1}$$

where η is the viscosity of the liquid.

Lee *et al.* [15] and Lee & Kim [16] used a commercial rheometer (AR 2000, TA instruments) whose operational torque range was between 0.1 and 200 mN m, with an angular velocity between 10^{-8} and 300 rad s^{-1}. They studied surfaces presenting well-regulated post and grate structures. The samples were created by photolithography and deep reactive etching on a silicon wafer. The grates were designed to be concentric so that they were parallel to the liquid flow in the rheometer system, and the posts had a circular cross section and were distributed in a square lattice. They studied the effective slip length versus the gas fraction (solid fraction) and also the value of the effective slip length versus the pitch value. In figure 6, the measured effective slip length for a fixed value of the gas

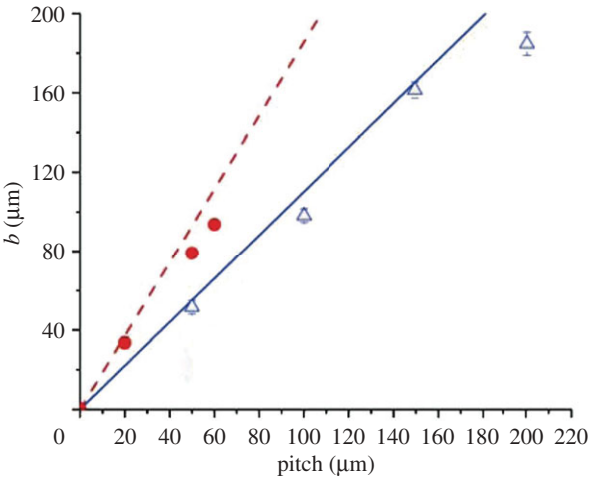

Figure 6. The effect of the pitch on the slip length with a gas fraction fixed at 98% [15]. The solid line represents theory for grates [11]; dashed line, theory for posts [13]; triangles, experimental data for grates [15]; circles, experimental data for posts [15]. Reproduced with permission. (Online version in colour.)

fraction (98%) is shown, but with varying pitches of 20, 50 and 60 μm for a post and 50, 200 and 250 μm for grates. The depth for each sample was maintained to be the same as the varying pitch. The slip length increases linearly with the pitch for both posts and grates, which is in agreement with the theoretical predictions. This result illustrates that as the pitch is larger, the produced slip length is larger with a limitation fixed by the condition for the wetting transition.

Bocquet *et al.* [20] reported some questions about the accuracy of the measurements of the slip length using a rheometer. They showed that the uncertainty in the measurements can be of the same order of magnitude as the slip length.

(*b*) *Particle image velocimetry experiments*

In order to measure the flow in the vicinity of such surfaces, particle image velocimetry has been used by several authors [21–23]. In such techniques, the velocity profile of the liquid can be measured with high accuracy, and the slip length can be extracted from the equation [24] $b = v_s/\partial v_s/\partial z$, where v_s and $\partial v_s/\partial z$ are the velocity and the shear rate close to the surface.

The common set-up used in particle image velocimetry is based on the measurement of the velocity of fluorescent particles embedded in water. An example of these set-ups is used by Joseph *et al.* [22] to study water flow on a superhydrophobic surface made of a carbon nanotube (CNT) forest. These CNTs were embedded in a microfluidic set-up with a microchannel, as shown in figure 7. A pressure-driven flow is induced by controlling inlet and outlet pressure. Usually, the observation was made using an objective with a large numerical aperture (NA = 1.3) to achieve a narrow depth of field. A scan in the vertical direction allows a change of the position of the focal plane and measurement of the velocity profile $v(z)$ in the whole microchannel. The focal plane was controlled with a piezo.

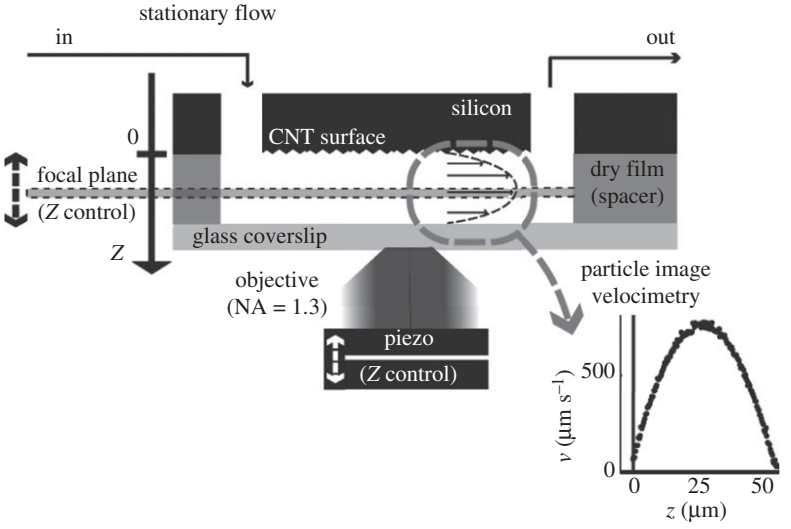

Figure 7. Experimental particle image velocimetry set-up used by Joseph *et al.* [22]. A pressure-driven flow is conducted in a microchannel made from glass/carbon nanotube forest surfaces. The focal plane Z is controlled with a piezo. Velocimetry is measured using particle image velocimetry over the whole channel depth. Reproduced with permission.

On CNT forest surfaces, Joseph *et al.* [22] measured the velocity profile and extracted the slip length by fitting the data using the predicted Poiseuille profile. They studied flow on CNT surfaces in the Cassie state (trapped air pocket) and also surfaces in the Wenzel state where the CNT surfaces are impregnated. (Descriptions of various wetting regimes can be found in Nosonovsky & Bhushan [25].) In the latter surface, the effective solid–liquid interface is fixed at the mean position between the top and the bottom of the CNT. The characteristic lateral scale of these surfaces is related to the nanotube interdistance, which can be tuned during the deposition process of the nanotube on the substrate. The slip length was measured for a surface having a lateral characteristic length between 1 and 6 μm. For the surfaces prepared in the Cassie state, the slip length increases with increasing length scale L, as shown in figure 8. However, for the surfaces that are in the Wenzel state, the slippage is strongly reduced owing to the absence of trapped air on the surface and thus increases of liquid–solid friction. The error bars on figure 8 correspond to dispersion in the measurements.

Ou & Rothstein [21] used particle imaging on superhydrophobic surfaces fabricated from silicon wafers using photolithography and designed to incorporate precise patterns of micrometre-sized ridges aligned in the flow direction. A schematic of the surface is presented in figure 9*a*. In figure 9*b*, the velocity profile across two different microchannels is shown, both with $H = 80\,\mu\text{m}$ height. For one of them, the superhydrophobic surface consists of $w = 30\,\mu\text{m}$ wide microridges spaced at $d = 30\,\mu\text{m}$, and for the second surface, $w = 30\,\mu\text{m}$ and $d = 60\,\mu\text{m}$. As given by the boundary conditions, the velocity profile on the microridges is zero (no-slip). Above the microridges, the velocity increases to a maximum near the centre line and returns to zero at the opposite surface,

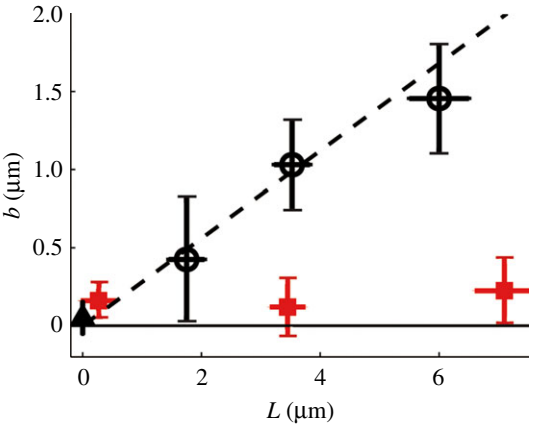

Figure 8. Measured slip length on the CNT surface as a function of the characteristic lateral length scale L of the underlying CNT forests. Circles, surfaces in the Cassie state; squares, surfaces in the Wenzel state. The dotted line is the theoretical prediction for the slip length [22]. Reproduced with permission. (Online version in colour.)

which is a smooth surface with no-slip boundary conditions. However, when the measurement was on the shear-free air–water interface (between the ridges), the velocity is not equal to zero, and it is maximum for measurements at the centre of the shear-free interface. For the surface having microridges ($w = 30\,\mu$m and $d = 60\,\mu$m), the slip length extracted from the measurement is found to be equal to $b = 7.5\,\mu$m. The measurements made are in agreement with their simulations, as shown in figure 9*b*.

In summary, particle image velocimetry is a direct technique that studies liquid flow close to solid surfaces. It allows direct access to the velocity profile and extraction of the slip length with high accuracy. It was used to measure the effective slip length on different superhydrophobic surfaces.

(*c*) *Pressure-drop experiments*

In such experiments, the slip length is extracted from the measurements of pressure drop as a function of the flow rate in a microchannel [21,26]. Using the Navier boundary conditions, the volume flow rate per unit length q of the fluid between two infinite parallel plates separated by a height H is given by

$$q = \frac{H^3}{4\eta}\left(-\frac{\mathrm{d}p}{\mathrm{d}z}\right)\left[\frac{1}{3} + \frac{b}{H+b}\right], \tag{3.2}$$

where $(\mathrm{d}p/\mathrm{d}z)$ is the pressure gradient and b is the effective slip length (in the above expression, one of the surfaces is supposed to be superhydrophobic).

Ou & Rothstein [21] showed that the presence of an air–water interface on superhydrophobic surfaces induces less resistance on the flow compared with no-slip surfaces. They measured the drag reduction coefficient,

$$D_{\mathrm{R}} = \frac{\Delta p_{\text{no-slip}} - \Delta p_{\mathrm{SH}}}{\Delta p_{\text{no-slip}}}, \tag{3.3}$$

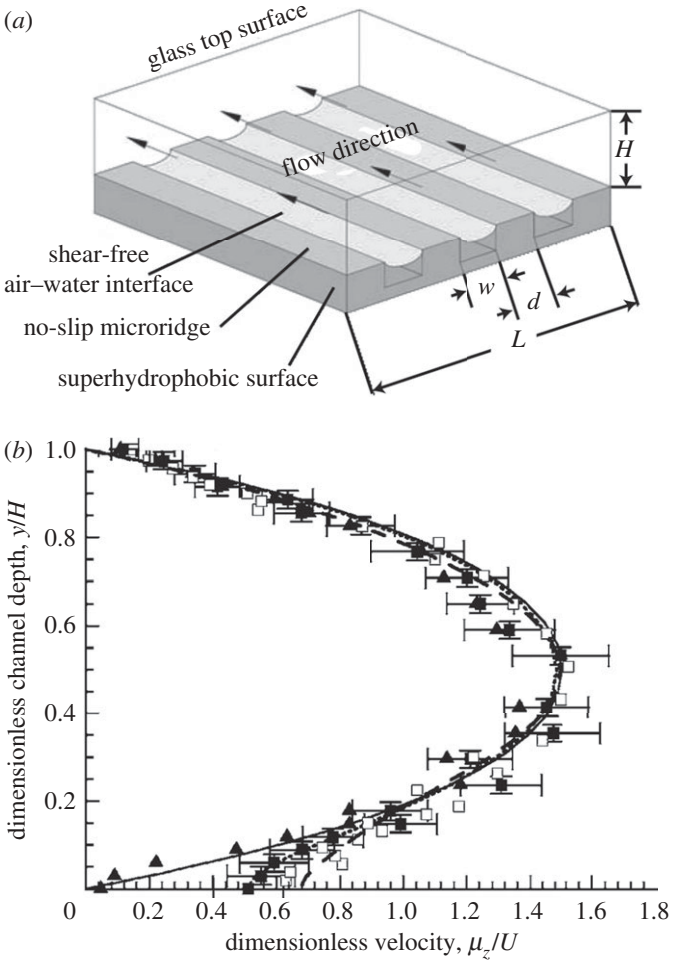

Figure 9. (*a*) Schematic of the superhydrophobic surface to perform particle image velocimetry for measuring the slip length of water on these surfaces and (*b*) measurements of the velocity profile and comparison with numerical simulations for the flow on the microchannel. The data are for measurements for the vertical profile above the centre of the microridges (triangles), above the centre of the free-shear interface for the surface having microridges spaced by $d = 30\,\mu\text{m}$ (filled squares) and above the centre of the shear-free interface for the surface $d = 60\,\mu\text{m}$ (open squares). Reproduced with permission from [21].

where Δp_{SH} is the experimentally measured pressure drop on the superhydrophobic surfaces and $\Delta p_{\text{no-slip}}$ is the pressure drop for flow over a no-slip surface at the same flow rate.

An important consequence of the surface slip is the reduction of drag or pressure drop, which is directly measured by the flow-rate measurement in the experiment. They achieved, in some cases, drag reduction $D_{\text{R}} > 40\%$, which corresponds to a slip length larger than $20\,\mu\text{m}$. They have also shown that the drag reduction increased with increasing shear-free area. Figure 10 shows the drag reduction versus the fraction of the free-shear area.

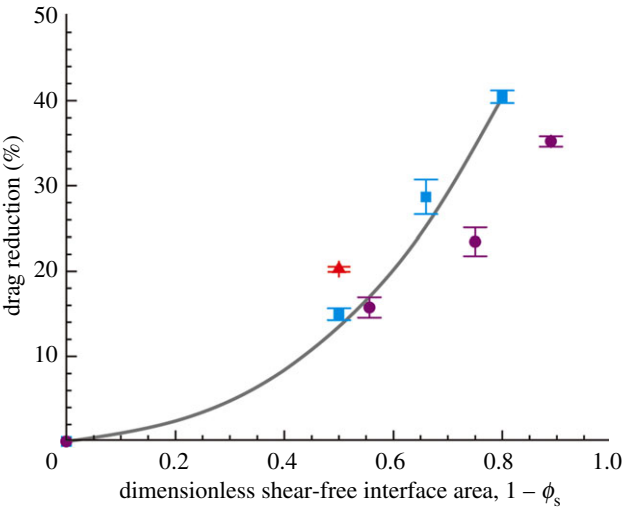

Figure 10. The drag reduction as a function of the fraction of the shear-free interface area. The solid line is a prediction of fluid dynamics simulations for a surface of 20 µm microridges for various space widths [8]. Reproduced with permission. (Online version in colour.)

(*d*) *Surface force apparatus experiments*

Steinberger *et al.* [27] used a homemade SFA to study the liquid flow on superhydrophobic surfaces. They used a microstructured surface embedded with a square lattice of calibrated cylindrical holes. The plain microstructured surface was a hydrophilic surface wetted by water in the Wenzel regime where the holes were filled by water. Silanized microstructured surfaces are superhydrophobic surfaces, and the wetting state is the Cassie regime with air bubbles trapped in the cylindrical holes. They studied the flow of a mixture water and glycerol (viscosity $\eta = 39 \pm 2$ mPa s) using the dynamic SFA. The dynamic SFA measures the real $G'(\omega)$ and the imaginary part $G''(\omega)$ of the complex force acting on the surfaces when the sphere of the SFA is vibrated in the normal direction with a frequency $\omega/2\pi$.

The imaginary part of the complex force response $G''(\omega)$ is the viscous damping of the liquid flow, and it depends linearly on the gap for a distance larger than the slip length. The linear extrapolation of the inverse of the viscous damping $G''^{-1}(\omega)$ intercepts the distance axis at a position given by the effective slip length. The real part $G'(\omega)$ is related to the elastic interaction owing to the confined liquid.

For the surface wetted in the Wenzel state, some of the liquid inside the holes contributes to the flow. The real no-slip plane lies underneath the top of the wall, and thus the measured $G''^{-1}(\omega)$ gives an effective slip length of $b = 105$ nm (figure 11*a*). The real part $G'(\omega)$ is equal to zero for all distances, as there is no elastic deformation of the surface (figure 11*b*).

For the surface wetted in the Cassie state, the presence of air bubbles trapped in the holes reduces the value of the effective slip length, as shown in figure 11*c*. The asymptote of the inverse of the viscous damping intercepts the distance axis at a distance of $b = 20$ nm. The real part $G'(\omega)$ of the response is not zero, and it

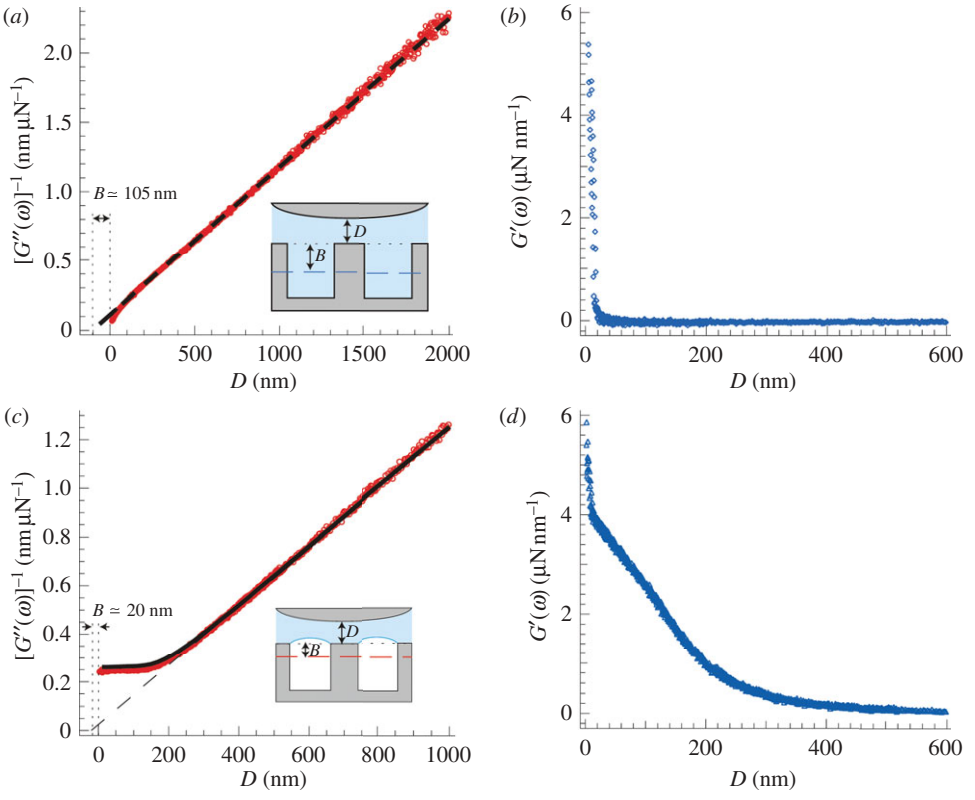

Figure 11. Flow between a Pyrex sphere and a textured microstructured plane (see insets). In (a,b), the surface is hydrophilic; the liquid fills the holes. In (c,d), the surface is superhydrophobic and the liquid does not fill the holes. (a,c) Show the evolution of the inverse of the viscous damping $G''^{-1}(\omega)$ as a function of the distance between the surfaces. The far-field asymptote (dashed line) allows the determination of the slip length. (b,d) Show the evolution of the elastic part $G'(\omega)$ as a function of the distance. Reproduced with permission from [27]. (Online version in colour.)

shows the contribution of the bubbles that deform under the pressure induced by the flow (figure 11*d*). This elastic response confirms the presence of the bubbles in the holes.

Steinberger *et al.* [27,28] and Hyväluoma & Harting [29] studied the influence of the shape of the meniscus (contact angle of the bubbles) on the slip length. Their numerical calculations showed a decrease of the effective slip length owing to the meniscus curvature (figure 12). A huge decrease of the effective slip length is obtained for menisci that correspond to a contact angle $\theta > 45°$. The obtained results are in agreement with the predictions of Richardson [30], which shows that the boundary conditions for a shear-free interface become no-slip if the surface is sufficiently rough.

In summary, this SFA experiment pointed out the role of the liquid–gas menisci on the boundary conditions of the liquid flow. The gas trapped at the solid surface can act as an anti-lubricant and promote high friction. These results cast some doubts on whether the presence of nanobubbles can be responsible for the large slip length on a smooth hydrophobic surface.

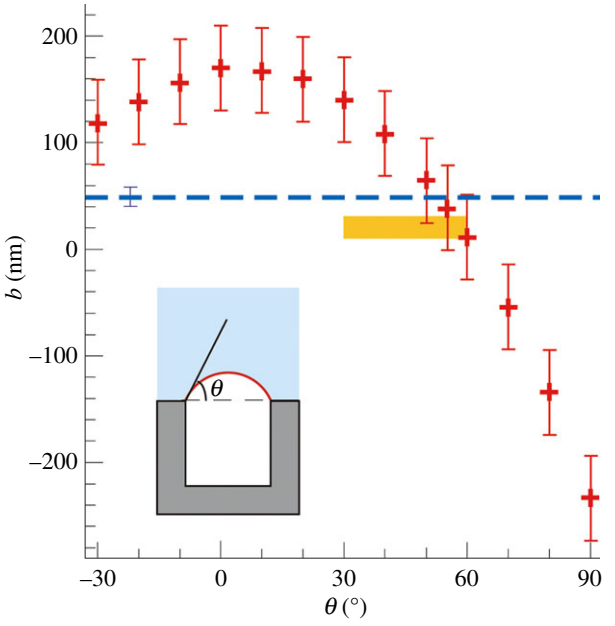

Figure 12. Evolution of the slip length with a menisci shape. The dashed line corresponds to a numerical value in the hydrophilic case when the liquid fills the holes. Reproduced with permission from [27]. (Online version in colour.)

(*e*) *Atomic force microscope experiments*

Bhushan *et al.* [31] have used a dynamic mode AFM experiment to measure slip length on hydrophobic and superhydrophobic surfaces (also see Wang & Bhushan [7]). Their experiments were calibrated using a hydrophilic surface (mica) where the no-slip boundary conditions were well known. In their experiment, a glass sphere of $42.4 \pm 0.8\,\mu$m diameter was glued to the end of a cantilever (figure 13*a*). The substrate sample was approached to the sphere at very low velocity, and the deflection signal was monitored as an indicator to determine a hard contact position. They measured, using a lock-in-amplifier, the amplitude and phase shift data as a function of piezo displacement during the cantilever approach to the hydrophilic, hydrophobic and superhydrophobic surfaces.

From the amplitude and phase, they extracted the total damping coefficient as a function of separation distance between the sphere and the sample surfaces [32],

$$1 + \frac{\gamma_H}{\gamma_0} = -\frac{A_0}{A}\sin(\varphi)\frac{Q_0}{\sqrt{1+Q_0^2} + 2(A_0/A)\cos(\varphi) + A_0^2/A^2\sqrt{1+Q_0^2}}, \tag{3.4}$$

where A_0 is the free oscillation amplitude of the cantilever far from the surface, while A is the amplitude of the cantilever at a given position, Q_0 is the quality factor of the cantilever far from the surface, φ is the phase shift at a given position and γ_0 is the bulk viscous damping coefficient far from the substrate surfaces.

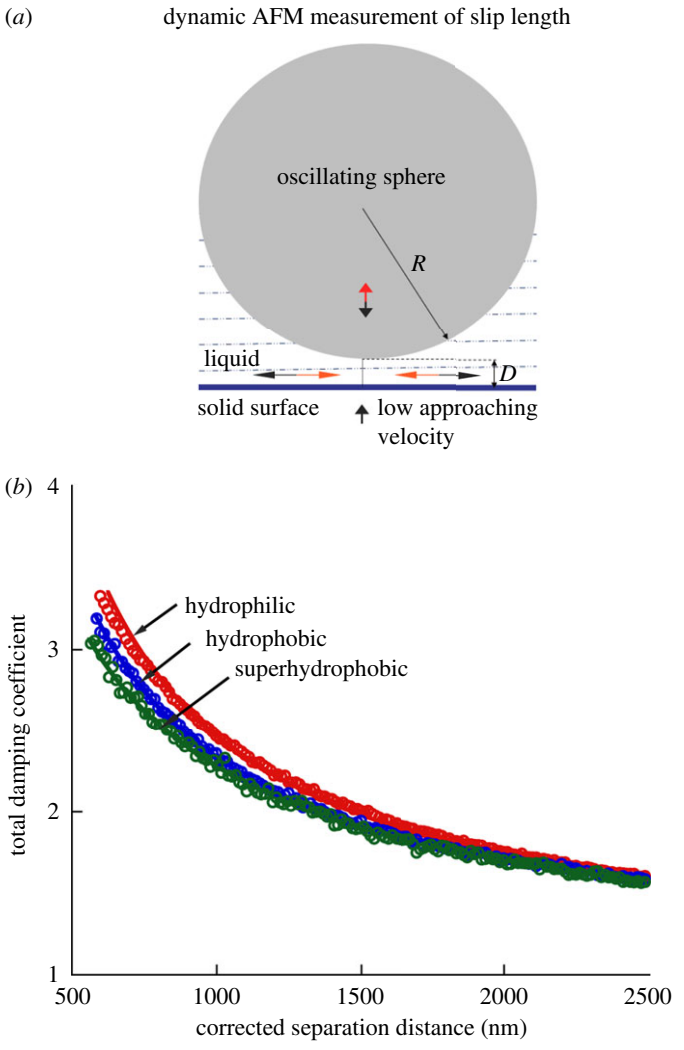

Figure 13. (*a*) A schematic of an oscillating sphere approaching a surface and profiles of the velocity amplitude of fluid flow with and without boundary slip. The arrows above and below the solid surface represent directions for fluid flow and relative movement of the sample surface to the sphere, respectively. (*b*) Total damping coefficient as a function of separation distance between the sphere and sample surfaces and corresponding fitting curves on the hydrophilic, hydrophobic and superhydrophobic surfaces. Adapted from [31]. (Online version in colour.)

The damping coefficients versus distance are shown in figure 13*b*. For a given separation distance, the total damping coefficient decreases with the sequence of hydrophilic, hydrophobic and superhydrophobic surfaces, indicating an increasing degree of boundary slip with increasing hydrophobicity. For each surface, the calculated damping coefficient increases with decreasing separation distance.

In the analysis of the experiment of Bhushan *et al.* [31] to eliminate the influence of surface roughness of hydrophobic and superhydrophobic surface on boundary slip, they took the mean surface as a virtual plane where the solid–liquid interface is located.

To evaluate the degree of the slip length at the solid–liquid interfaces of the three surfaces, the measured hydrodynamic damping coefficients were fitted using

$$\gamma_{\mathrm{H}} = \frac{6\pi R^2 \eta}{D} f^*, \tag{3.5a}$$

where f^* is the correction function that takes into account the boundary slip on the surfaces, given by Vinogradova [33],

$$f^* = \frac{1}{4} \quad 1 + \frac{6D}{4b}\left[\left(1 + \frac{D}{4b}\right)\ln\left(1 + \frac{4b}{D}\right) - 1\right]\Bigg\}, \tag{3.5b}$$

where D is the closest separation distance between the sphere and the solid surface, η is the viscosity of the liquid and γ_{H} is the hydrodynamic damping coefficient. Slip lengths of about 43 and 236 nm are obtained on hydrophobic and superhydrophobic surfaces, which indicate that the slip length increases with increasing hydrophobicity.

In this experiment [31], the authors have assumed that the boundary slip is described by the Vinogradova equation shown above. More recently, Asmolov *et al.* [34] showed that on textured superhydrophobic surfaces, the effective slip length is not independent of the distance in the drainage experiments. Asmolov *et al.* [34] suggested a new expression to evaluate the slip length on textured superhydrophobic surfaces, and it will be useful to check such expressions in forthcoming AFM experiments.

4. Summary and outlook

This paper presents a review of different techniques for measurement of the large slip length on superhydrophobic surfaces. First, the theoretical models used to calculate the effective slip length on superhydrophobic surfaces in different configurations of liquid flow are presented. Then, details of different experimental techniques are presented that are used to measure the slip on these superhydrophobic surfaces.

Particle image velocimetry is a direct measurement of the slip length since it measures the velocity profile of the fluid in the vicinity of the superhydrophobic surfaces. The measurements in this case are also more local and can probe the liquid flow in different parts of the surface; on the shear-free part (liquid–gas interface) and also on the low-slip part (solid–liquid interface). The other techniques described in this review are indirect measurements. In these cases, the slip length is extracted from torque measurements (rheometry experiments), flow rate versus pressure-drop measurements (pressure-drop experiments) and from damping versus distance (SFA and AFM experiments). The rheometry and pressure-drop experiments are useful only for a large slip length due to the low resolution of such techniques. Furthermore, the measured flow is an average flow on the whole surface and on the whole gap of the microchannel. The SFA also provides an average value of the flow; however, it has the benefit of probing the flow at the nanoscale by changing the gap between the confining surfaces. The AFM experiments can provide local measurements of the boundary conditions by changing the probed position on the surfaces. They also have the benefit of controlling the gap of the flow (from a few of micrometres to nanometres), and produce measurements with high accuracy down to a few nanometres.

Although the field of slip of the liquid flow on a superhydrophobic surface has been extensively studied, as we have shown in this review; however, many challenges remain. It has been shown by the SFA experiments that the liquid–gas menisci on superhydrophobic surfaces play an important role on the boundary conditions of the liquid flow. The gas trapped at solid surfaces can act as an anti-lubricant and promote high friction. Therefore, controlling the shape of the meniscus will allow the tuning of the boundary conditions at the surface. This may be done by use of the electrowetting process, which is a promising technique [35,36].

Liquid flow at turbulent flow (high Reynolds numbers) is another interesting topic to be examined. For laminar flow, the reported slip was independent of flow rate; however, for turbulent flow, recent results demonstrated that the slip increased with increasing Reynolds number, and substantial reduction of friction coefficient was also reported [37]. The upper value of the slip and the maximum drag reduction is still unknown in the high Reynolds number regime. The role of the curvature of the shear-free interface on the slip in turbulent flow needs to be studied.

The authors thank Yunlu Pan for critical reading of the paper.

References

1 Churaev, N. V., Sobolev, V. D. & Somov, A. N. 1984 Slippage of liquids over lyophobic solid-surfaces. *J. Colloid Interf. Sci.* **97**, 574–581. (doi:10.1016/0021-9797(84)90330-8)

2 Lauga, E., Brenner, M. P. & Stone, H. A. 2005 Microfluidics: the no-slip boundary condition. In *Handbook of experimental fluid dynamics*, ch. 15. New York, NY: Springer.

3 Neto, C., Evans, D. R., Bonaccurso, E., Butt, H.-J. & Craig, V. S. J. 2005 Boundary slip in Newtonian liquids: a review of experimental studies. *Rep. Prog. Phys.* **68**, 2859. (doi:10.1088/0034-4885/68/12/R05)

4 Maali, A. & Bhushan, B. 2008 Nanorheology and boundary slip in confined liquids using atomic force microscopy. *J. Phys.: Condens. Matter* **20**, 315201. (doi:10.1088/0953-8984/20/31/315201)

5 Bocquet, L. & Charlaix, E. 2010 Nanofluidics, from bulk to interfaces. *Chem. Soc. Rev.* **39**, 1073–1095. (doi:10.1039/b909366b)

6 Bocquet, L. & Barrat, J.-L. 2007 Flow boundary conditions from nano- to micro-scales. *Soft Matter* **3**, 685–693. (doi:10.1039/b616490k)

7 Wang, Y. & Bhushan, B. 2009 Boundary slip and nanobubble study in micro/nanofluidics using atomic force microscopy. *Soft Matter* **6**, 29–66. (doi:10.1039/b917017k)

8 Rothstein, J. P. 2010 Slip on superhydrophobic surfaces. *Annu. Rev. Fluid Mech.* **42**, 89–109. (doi:10.1146/annurev-fluid-121108-145558)

9 Philip, J. R. 1972 Flows satisfying mixed no-slip and no-shear conditions. *Z. Angew. Math. Phys.* **23**, 353–372. (doi:10.1007/BF01595477)

10 Philip, J. R. 1972 Integral properties of flows satisfying mixed no-slip and no-shear conditions. *Z. Angew. Math. Phys.* **23**, 960–968. (doi:10.1007/BF01596223)

11 Lauga, E. & Stone, H. A. 2003 Effective slip in pressure-driven stokes flow. *J. Fluid Mech.* **489**, 55–77. (doi:10.1017/S0022112003004695)

12 Cottin-Bizonne, C., Barentin, C., Charlaix, É., Bocquet, L. & Barrat, J.-L. 2004 Dynamics of simple liquids at heterogeneous surfaces: molecular-dynamics simulations and hydrodynamic description. *Eur. Phys. J. E* **15**, 427–438. (doi:10.1140/epje/i2004-10061-9)

13 Ybert, C., Barentin, C., Cottin-Bizonne, C., Joseph, P. & Bocquet, L. 2007 Achieving large slip with superhydrophobic surfaces: scaling laws for generic geometries. *Phys. Fluids* **19**, 123601. (doi:10.1063/1.2815730)

14 Davis, A. M. J. & Lauga, E. 2010 Hydrodynamic friction of fakir-like superhydrophobic surfaces. *J. Fluid Mech.* **661**, 402–411. (doi:10.1017/S0022112010003460)

15 Lee, C., Choi, C.-H. & Kim, C.-J. 2008 Structured surfaces for a giant liquid slip. *Phys. Rev. Lett.* **101**, 064501. (doi:10.1103/PhysRevLett.101.064501)
16 Lee, C. & Kim, C.-J. 2009 Maximizing the giant liquid slip on superhydrophobic microstructures by nanostructuring their sidewalls. *Langmuir* **25**, 12 812–12 818. (doi:10.1021/la901824d)
17 Lee, C. & Kim, C.-J. 2011 Influence of surface hierarchy of superhydrophobic surfaces on liquid slip. *Langmuir* **27**, 4243–4248. (doi:10.1021/la104368v)
18 Ming, Z., Jian, L., Chunxia, W., Xiaokang, Z. & Lan, C. 2011 Fluid drag reduction on superhydrophobic surfaces coated with carbon nanotube forests (CNTs). *Soft Matter* **7**, 4391–4396. (doi:10.1039/c0sm01426e)
19 Choi, C.-H. & Kim, C.-J. 2006 Large slip of aqueous liquid flow over a nanoengineered superhydrophobic surface. *Phys. Rev. Lett.* **96**, 066001. (doi:10.1103/PhysRevLett.96.066001)
20 Bocquet, L., Tabeling, P. & Manneville, S. 2006 Comment on 'Large slip of aqueous liquid flow over a nanoengineered superhydrophobic surface'. *Phys. Rev. Lett.* **97**, 109601. (doi:10.1103/PhysRevLett.97.109601)
21 Ou, J. & Rothstein, J. P. 2005 Direct velocity measurements of the flow past drag-reducing ultrahydrophobic surfaces. *Phys. Fluids* **17**, 103606. (doi:10.1063/1.2109867)
22 Joseph, P., Cottin-Bizonne, C., Benoît, J.-M., Ybert, C., Journet, C., Tabeling, P. & Bocquet, L. 2006 Slippage of water past superhydrophobic carbon nanotube forests in microchannels. *Phys. Rev. Lett.* **97**, 156104. (doi:10.1103/PhysRevLett.97.156104)
23 Truesdell, R., Mammoli, A., Vorobieff, P., van Swol, F. & Brinker, C. J. 2006 Drag reduction on a patterned superhydrophobic surface. *Phys. Rev. Lett.* **97**, 044504. (doi:10.1103/PhysRevLett.97.044504)
24 Navier, C. L. M. H. 1823 Mémoire sur les lois du mouvement des fluids. *Mem. Acad. R. Sci. Inst. France* **6**, 389–416.
25 Nosonovsky, M. & Bhushan, B. 2008 *Multiscale dissipative mechanisms and hierarchical surfaces: friction, superhydrophobicity, and biomimetics*. Heidelberg, Germany: Springer.
26 Ou, J., Perot, B. & Rothstein, J. P. 2004 Laminar drag reduction in microchannels using ultrahydrophobic surfaces. *Phys. Fluids* **16**, 4635. (doi:10.1063/1.1812011)
27 Steinberger, A., Cottin-Bizonne, C., Kleimann, P. & Charlaix, E. 2007 High friction on a bubble mattress. *Nat. Mater.* **6**, 665–668. (doi:10.1038/nmat1962)
28 Steinberger, A., Cottin-Bizonne, C., Kleimann, P. & Charlaix, E. 2008 Nanoscale flow on a bubble mattress: effect of surface elasticity. *Phys. Rev. Lett.* **100**, 134501. (doi:10.1103/PhysRevLett.100.134501)
29 Hyväluoma, J. & Harting, J. 2008 Slip flow over structured surfaces with entrapped microbubbles. *Phys. Rev. Lett.* **100**, 246001. (doi:10.1103/PhysRevLett.100.246001)
30 Richardson, S. 1973 On the no-slip boundary condition. *J. Fluid. Mech.* **59**, 707–719. (doi:10.1017/S0022112073001801)
31 Bhushan, B., Wang, Y. & Maali, A. 2009 Boundary slip study on hydrophilic, hydrophobic, and superhydrophobic surfaces with dynamic atomic force microscopy. *Langmuir* **25**, 8117–8121. (doi:10.1021/la900612s)
32 Jai, C., Cohen-Bouhacina, T. & Maali, A. 2007 Analytical description of the motion of an acoustic-driven atomic force microscope cantilever in liquid. *Appl. Phys. Lett.* **90**, 113512. (doi:10.1063/1.2713860)
33 Vinogradova, O. I. 1995 Drainage of a thin liquid-film confined between hydrophobic surfaces. *Langmuir* **11**, 2213–2220. (doi:10.1021/la00006a059)
34 Asmolov, E. S., Belyaev, A. V. & Vinogradova, O. I. 2011 Drag force on a sphere moving toward an anisotropic superhydrophobic plane. *Phys. Rev. E* **84**, 026330. (doi:10.1103/PhysRevE.84.026330)
35 Bhushan, B. & Ling, X. 2008 Integrating electrowetting into micromanipulation of liquid droplets. *J. Phys: Condens. Matter* **20**, 485009. (doi:10.1088/0953-8984/20/48/485009)
36 Bhushan, B. & Pan, Y. 2011 Role of electric field on surface wetting of polystyrene surface. *Langmuir* **27**, 9425–9429. (doi:10.1021/1.2016369)
37 Daniello, R. J., Waterhouse, N. E. & Rothstein, J. P. 2009 Drag reduction in turbulent flows over superhydrophobic surfaces. *Phys. Fluids* **21**, 085103. (doi:10.1063/1.3207885)